sustainability

IMPACT FACTOR 3.3

CITESCORE 7.7

Article

Modeling and Analysis of a Novel Levitation Magnet with Damping Coils for High-Speed Maglev Train

Shanqiang Fu, Zigang Deng, Weitao Han, Xinmai Gao and Ying Zhou

MDPI

https://doi.org/10.3390/su16125247

sustainability

MDPI

Article

Modeling and Analysis of a Novel Levitation Magnet with Damping Coils for High-Speed Maglev Train

Shanqiang Fu [1,2,3], Zigang Deng [1,*], Weitao Han [2,3,*], Xinmai Gao [2,3] and Ying Zhou [2,3]

[1] State Key Laboratory of Rail Transit Vehicle System, Southwest Jiaotong University, Chengdu 610031, China; sf-fushanqiang@cqsf.com
[2] CRRC Qingdao Sifang Company Ltd., Qingdao 266111, China; gaoxinmai@cqsf.com (X.G.); sfzhouying@cqsf.com (Y.Z.)
[3] State Key Laboratory of High-Speed Maglev Transportation Technology, Qingdao 266111, China
* Correspondence: deng@swjtu.edu.cn (Z.D.); hanweitaotao@163.com (W.H.)

Abstract: In this work, a novel levitation magnet with damping coil is proposed to address the existing issues and improve reliability. The fault mechanism of the existing magnet is analyzed and validated using a coupling model combined with inductive voltage experiments. The magnetic yoke with damping coils is designed and the equivalent magnetic circuit (EMC) model of the magnet is established. The nonlinearity of magnetic materials and the magnetic flux fluctuation due to the tooth-slot effect are considered in the EMC model. Simultaneously, the transient finite element (FEM) model is built. The magnetic flux of yoke, the inductive current of the damping coil, and the magnetic force are analyzed. A good agreement is found between EMC and FEM. Additionally, the static magnetic force is tested on the magnet test platform to validate EMC and FEM models. Results reveal that compared with the existing magnet, the magnetic flux fluctuation with damping coils is significantly reduced, and the inductive voltages with the damping coil are significantly decreased. The novel magnet with damping coils featuring excellent magnetic characteristics is more advantageous for the system's security and durability.

Keywords: damping coils; magnetic circuit; inductive voltage; magnetic flux; magnetic force

Citation: Fu, S.; Deng, Z.; Han, W.; Gao, X.; Zhou, Y. Modeling and Analysis of a Novel Levitation Magnet with Damping Coils for High-Speed Maglev Train. *Sustainability* **2024**, *16*, 5247. https://doi.org/10.3390/su16125247

Academic Editor: Jiageng Ruan

Received: 15 April 2024
Revised: 15 June 2024
Accepted: 18 June 2024
Published: 20 June 2024

1. Introduction

Nowadays, magnetic levitation (maglev) technology has been widely commercialized in high-speed machinery due to its advantages of no friction, micro-vibration, long life, high precision, and so on. As a core component for rotating machinery, magnetic bearings are generally applied to support high-speed rotor contactless, such as maglev flywheels, maglev control moment gyroscopes, and maglev motors [1–4]. Regarding linear motion, the magnet and linear motors are combined and applied; the magnet realizes levitation and the linear motor is used for propulsion, such as the maglev train and the maglev elevator. So far, maglev train technology has been researched for a long time in the world. Several countries have successfully implemented maglev projects for commercial operation, while others are currently in the planning stages for similar ventures, such as China, Germany, Japan, South Korea, etc. [5–8]. According to operating speeds, the maglev train can be classified into middle–low- and high-speed types. The maximum speed of the middle–low-speed maglev train approaches 200 km/h. A U-type magnet has been designed to achieve integrated levitation and guidance. Here, the levitation is actively controlled to maintain stability and the guidance is passive due to smaller lateral interference forces at lower speeds [9–11]. The maximum speed of the high-speed maglev trains is over 300 km/h, even reaching 600 km/h. At present, there are main two technical routes: superconducting electrodynamic suspension (SCEDS) vehicles from Japan and electromagnetic suspension (EMS) Transrapid technology from Germany. SCEDS vehicles achieve passive levitation and guidance via the passive repulsive forces generated by the dynamic interaction between the superconducting

magnets and the ground coils. It is crucial to design the superconducting magnet itself and match the relationship with the ground coils to ensure stable levitation [12–14]. The SCEDS vehicle L0 in Japan is in the trial operation stage and its maximum experiment speed reaches 603 km/h, but it is not available commercially yet. At present, the technical route of EMS is most mature and the EMS Transrapid TR08 manufactured by German firms has been operating commercially for nearly 20 years in Shanghai, China. The maximum experiment speed reaches 505 km/h and the maximum operation speed reaches 430 km/h. The levitation and guidance functions are achieved through active magnetic attraction forces generated by corresponding magnets, which are dynamically controlled to ensure stability, especially under the significant vertical and lateral loads experienced at high speeds [15–17]. The active electromagnetic control plays an important role in maintaining the stability and comfort of the vehicle, so many advanced levitation and guidance control algorithms have been researched and proposed by scholars [18,19].

Regardless of the type of maglev train, as the core executive component, the magnets play a crucial role in the support of vehicle and levitation stability. This work focuses on analyzing the levitation magnet of the high-speed EMS type. The operational load is significantly complex and demanding at high speeds, necessitating higher carrying capacity and reliability. Therefore, it is important to model and analyze the levitation magnet for the design and optimization of the levitation system. Magnetic modeling and analysis methods mainly include the EMC method and the FEM method. The FEM method has high accuracy but poor efficiency, making it unsuitable for real-time analysis and rapid optimization. The EMC method has a high computing speed, making it convenient for the analysis and optimization of real-time dynamic characteristics. However, traditional EMC accuracy is relatively unsatisfactory due to constant relative permeability associated with the magnetic material, and the impact of magnetic saturation or even the reluctance of the magnetic material is ignored [20,21]. To address this issue, the reluctances and nonlinearity properties of magnetic materials are considered when the new EMC models are built in [22,23]. By incorporating the magnetization curve (BH curve) of the magnetic conductive material, the solution accuracy of magnetic force is greatly improved, and the range of application is increased. Therefore, the new EMC method is used as a reference in this paper. In addition, damping is an important parameter related to the system stability in high-speed machinery. In [24,25], the active and passive damping systems are designed to suppress high-speed rotor vibration and achieve improved results. In [26,27], the passive dampers based on eddy current effects are investigated to enhance the stability of the high-temperature conductor (HTS) maglev system. However, there is limited research on the damping design of the levitation magnet for the high-speed EMS train owing to the active control applied. Meanwhile, the active control of the loop circuit cannot suppress the magnetic flux fluctuation of each magnet pole caused by its own structure and power supply, which can lead to the magnet pole failure during operation. In this paper, the passive damping coils are designed and investigated to protect the magnet pole from overvoltage damage.

As Figure 1 shows, the levitation magnet with the high-speed EMS train includes 12 magnet poles with an N/S alternating polarity. The adjacent magnet poles are connected by magnetic yokes supported by torsion spring, and the magnetic field forms a loop through the stator core. The magnetic yokes are formed using laminated silicon steel sheets. The magnetic field between the magnet and long stator generates an attraction force, allowing the levitation function to be achieved. The 12 magnet poles are divided into left and right groups, each powered separately by two controllers. This division generates two control loops, with each loop corresponding to two gap sensors. The sensors monitor the gap between the magnet and long stator in real time and transmit these data back to the controller. Upon receiving this feedback, the controller calculates the appropriate control strategy and adjusts the current supplied to the magnet accordingly to achieve dynamic and stable suspension.

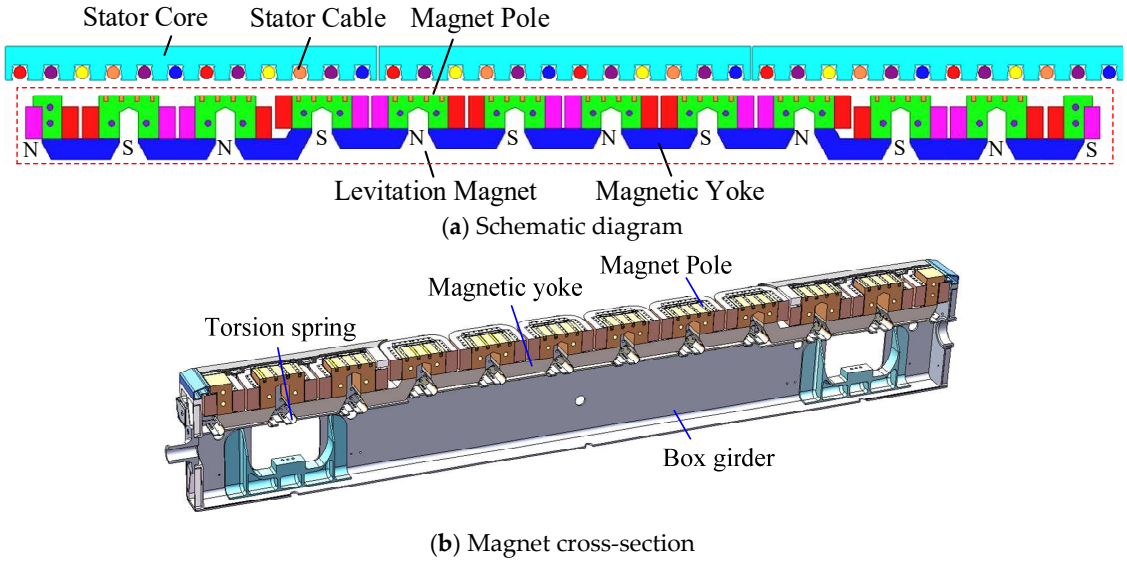

Figure 1. Levitation magnet and long stator.

The magnet pole, a crucial component of the powered excitation in magnet, as shown in Figure 2, comprises an iron core, coil, an insulation layer linear generator (LIG), and a flange plate. Similar to the magnetic yokes, the iron core is constructed by laminated silicon steel sheets. The upper and lower coils are connected and wound around the iron core, consisting of aluminum foil and insulating film arranged in alternating layers. An insulation layer is positioned between the iron core and the coil, playing an important role in protecting the coils from the short circuit failure with the iron core. Embedded within the iron core and sharing the magnetic field of the magnet pole, the LIG facilitates induction power generation. The magnet pole is encapsulated with epoxy resin and fixed on the girder through the aluminum alloy flange plate.

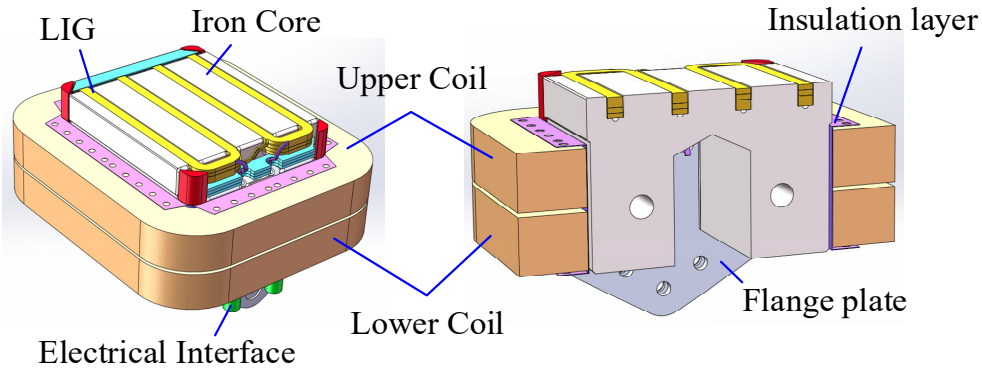

Figure 2. Magnet pole structure.

2. Magnet Pole Failure

During the long-term operation of the maglev train, the magnet pole frequently experiences insulation failure, resulting in increased maintenance workload and operating cost. After the large-scale disassembly of failure magnet poles, insulation fault points are identified and located on the insulation layer between the coils and the iron core, as illustrated in Figure 3. The damage of the insulation layer indicates that the voltage at this position exceeds the long-term operation voltage withstand test standard of 2.5 kV for the maglev train. While the maximum power supply voltage for the magnet is only 440 V. To analyze the mechanism of voltage formation, an electromagnetic coupling model of magnet is constructed, and tests are performed.

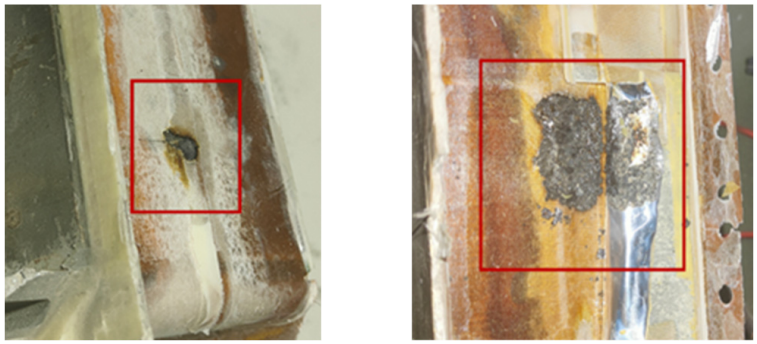

Figure 3. Insulation layer damage.

2.1. Electromagnetic Coupling Model

The electromagnetic coupling model of the half magnet is depicted in Figure 4. In a control circuit, six magnet poles are connected in series and powered by a controller. The coil can be equivalent to a series of resistors and inductors. Varistors are connected at points a and b to suppress the overloaded input voltage. As mentioned previously, the coil is composed of alternating layers of aluminum foil and insulation film, with an insulation layer between the coil and the iron core. Thus, parasitic capacitance exists between the coil and the iron core. When the coils are energized, the magnetic fluxes are generated by the magnet pole core, passing through the long stator, adjacent magnet pole cores, and magnetic yokes, and then they finally return to the initial position. If the magnetic flux in the magnetic circuit fluctuates, an inductive voltage will be induced from points U_1 to U_6 between the coil and the iron under electromagnetic coupling effects.

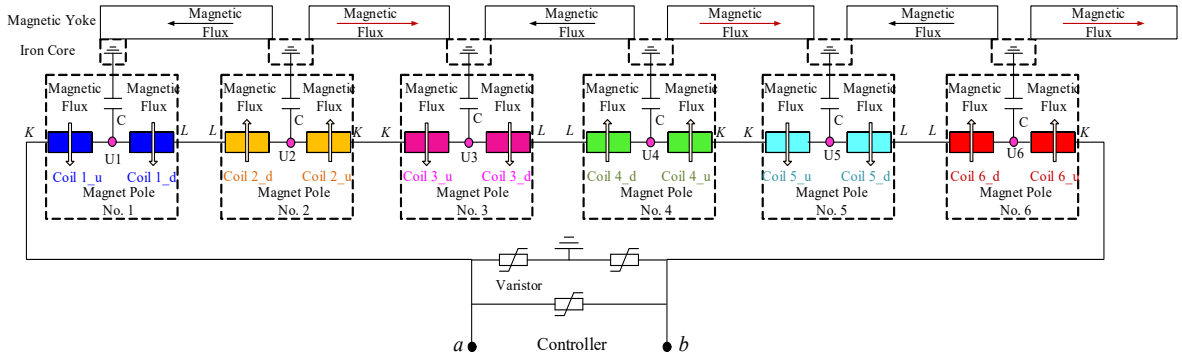

Figure 4. Coupling model of the magnet.

During high-speed operation, the primary factors contributing to magnetic flux fluctuation are the tooth-slot effect and high-frequency chopping power supply. The tooth-slot effect refers to the long stator structure shown in Figure 5. The reluctance of the air gap between the magnet pole and the long stator varies with the position of the magnet pole due to the tooth-slot structure of the long stator, thereby leading to magnetic flux fluctuations. Therefore, its fluctuation frequency is related to its operating speed. In addition, the high-frequency chopping power supply introduces high-frequency harmonics in the control loop of the magnet, also resulting in magnetic flux fluctuation. To further analyze the magnetic pole failure, the ground equivalent and actual vehicle tests are conducted.

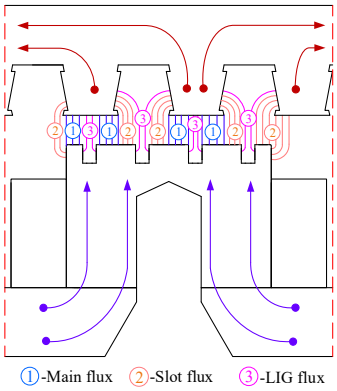

Figure 5. Flux distribution of magnet pole.

2.2. Inductive Voltage Test

As depicted in Figure 6, an equivalent ground test setup is established to facilitate the inductive voltage test and analysis. An actual controller is utilized for power supply, and the loop current is regulated to a nominal current of 25 A, augmented with a wave function with an amplitude of 10 A and a frequency of 1 Hz. This setup effectively simulates the inductive voltage characteristics of the actual operation. In the test results, the high voltages appeared at the points U_1 to U_6, especially the points U_3 to U_5. The inductive voltage result of magnet pole no. 4 (point U_4) is extracted and displayed in Figure 7. As the current increases, the inductive voltage increases. Two maximum voltage peaks are recorded separately at 2.6 kV and −2.9 kV, resulting in a maximum peak-to-peak value of 5.5 kV. This value surpasses the withstand test voltage standard of 2.5 kV, thus elevating failure risk.

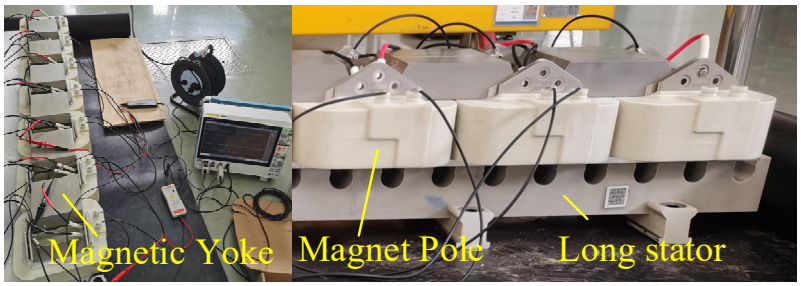

Figure 6. Equivalent ground test.

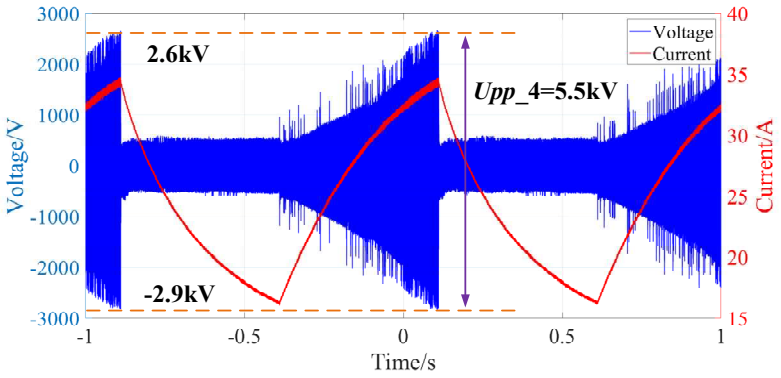

Figure 7. Inductive voltage of the equivalent ground test.

The inductive voltage of magnet pole no. 4 is tested at a lower speed of 50 km/h in the actual vehicle, and the results are displayed in Figure 8. The loop current is maintained at around 27 A with minimal fluctuation. At this moment, the two maximum voltage peaks

are 2.2 kV and −2.0 kV, and the maximum peak-to-peak value is 4.2 kV lower than that recorded in the ground test results.

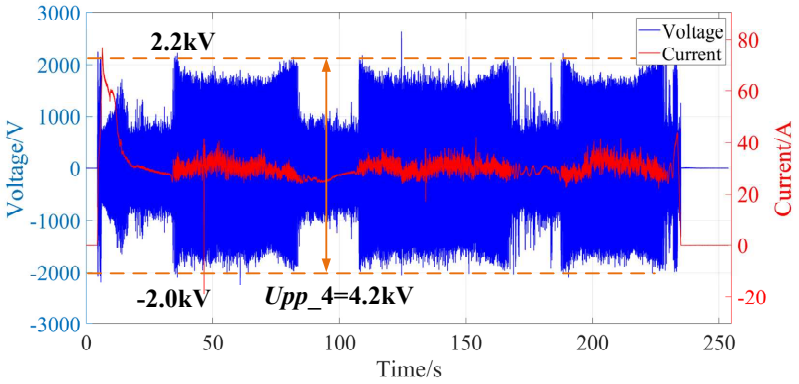

Figure 8. Inductive voltage of the real vehicle test.

3. Novel Magnet with Damping Coils

Based on failure analysis, the inductive voltage is intimately affected by magnetic flux fluctuation in the magnetic circuit. As aforementioned, the magnetic yoke is formed by laminated silicon steel sheets with excellent magnetic permeability and eddy current suppression abilities, making it difficult to suppress the magnetic flux fluctuation. Structural steel has been recommended for magnetic yoke once before. Although it can suppress magnetic flux fluctuation well by relying on the eddy current effect, the lower magnetic permeability will weaken the carrying capacity of the levitation magnet. Furthermore, the low-frequency magnetic flux regulation from the control current can also be suppressed, impacting the control system response. The magnetic flux fluctuation that generates a high inductive voltage falls in a higher frequency range over 100 Hz or even up to 1000 Hz. Subsequently, a novel magnet with damping coils is designed, as shown in Figure 9. The magnetic yoke is embedded with a damping coil to ensure external dimension. The coil is wound with copper enamel wire and connected in series with a resistor to form a closed loop. By adjusting the turns and resistance of the damping coil, high-frequency magnetic flux fluctuation can be suppressed while minimizing the impact on the control magnetic flux. In the following, the mathematic model of the novel magnet is established to efficiently analyze the electromagnetic characteristics.

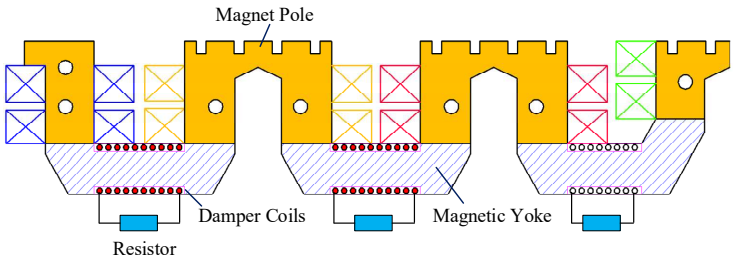

Figure 9. Schematic diagram of the novel magnet with damping coil.

4. Mathematic Model

4.1. Magnetic Circuit

To simplify the calculation model, only a half-magnetic circuit model is constructed, as the levitation magnet is controlled separately by the left and right loops. Meanwhile, to mitigate the impact of magnetic field coupling between the two loops, the seventh magnet pole is included in the half-model. The EMC model is illustrated in Figure 10. R_{aj} is the reluctance of the air gap between the magnet pole and stator. R_{si} is the reluctance of the stator core. R_{ei} is the reluctance of the magnet pole core magnetic yoke and R_{li} is the magnetic leakage reluctance between the adjacent magnet poles. ϕ_{aj}, ϕ_i, ϕ_{ei}, andϕ_{li} are the

magnetic fluxes corresponding to the reluctance values R_{aj}, R_{si}, R_{ei}, and R_{li}, respectively, andϕ_{pj} is the magnet pole flux. θ_j is the magnetomotive force of the pole coil and is equal to nI, where n is the number of pole coil turns and I is the control current. θ_{pj} is the magnetomotive force of the damping coil and equal to n_pI_{pi}, where n_p is the number of damping coil turns, and I_{pi} is the inductive current. Here, i = 1, 2…6, j = 1, 2…7. The resistance series connected with each damping coil is R_{dp}.

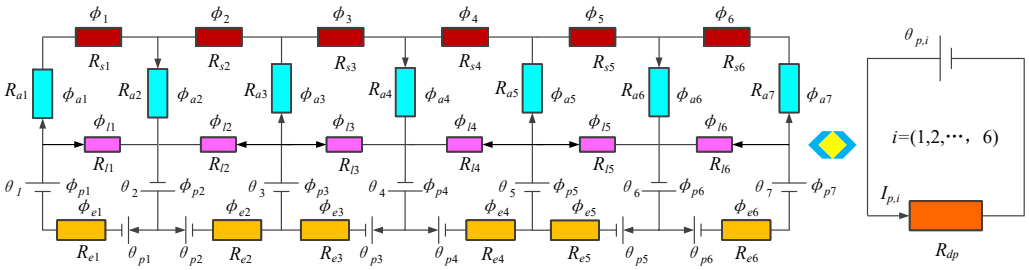

Figure 10. Equivalent magnetic circuit of 7 magnet poles.

The magnetic flux and magnetomotive force vectors are defined as follows:

$$\boldsymbol{\phi} = [\phi_1, \phi_{l1}, \phi_2, \phi_{l2} \cdots, \phi_6, \phi_{l6}]^T$$

$$\boldsymbol{\phi_s} = [\phi_1, \phi_2, \cdots, \phi_6]^T$$

$$\boldsymbol{\phi_a} = [\phi_1, \phi_{1+}\ \phi_2, \cdots, \phi_{5+}\ \phi_6, \phi_6]^T$$

$$\boldsymbol{\phi_e} = [\phi_{1+}\ \phi_{l1}, \phi_{2+}\ \phi_{l2}, \cdots, \phi_{6+}\ \phi_{l6}]^T$$

$$\boldsymbol{\phi_p} = [\phi_{1+}\ \phi_{l1}, \phi_{1+}\ \phi_{l1+}\ \phi_{2+}\ \phi_{l2}, \cdots, \phi_{5+}\ \phi_{l5+}\ \phi_{6+}\ \phi_{l6}, \phi_{6+}\ \phi_{l6}]^T$$

$$\boldsymbol{\theta} = [\theta_1, \theta_2, \cdots, \theta_7]^T$$

$$\boldsymbol{\theta_p} = [\theta_{p1}, \theta_{p2}, \cdots, \theta_{p6}]^T$$

The conversion relationship between magnetic flux vectors $\boldsymbol{\phi_p}$ and $\boldsymbol{\phi}$ is $\boldsymbol{\phi_p} = \mathbf{T}\boldsymbol{\phi}$. The conversion relationship between magnetic flux vectors $\boldsymbol{\phi_e}$ and $\boldsymbol{\phi}$ is $\boldsymbol{\phi_e} = \mathbf{T_e}\ \boldsymbol{\phi}$, where the matrix is

$$\mathbf{T} = \begin{bmatrix} 1 & 1 & & & & & & & & & & \\ 1 & 1 & 1 & 1 & & & & & & & & \\ & & 1 & 1 & 1 & 1 & & & & & & \\ & & & & 1 & 1 & 1 & 1 & & & & \\ & & & & & & 1 & 1 & 1 & 1 & & \\ & & & & & & & & 1 & 1 & 1 & 1 \\ & & & & & & & & & & 1 & 1 \end{bmatrix}$$

and the matrix is

$$\mathbf{T}_e = \begin{bmatrix} 1 & 1 & & & & & & & & & & \\ & & 1 & 1 & & & & & & & & \\ & & & & 1 & 1 & & & & & & \\ & & & & & & 1 & 1 & & & & \\ & & & & & & & & 1 & 1 & & \\ & & & & & & & & & & 1 & 1 \end{bmatrix}$$

According to the Kirchhoff voltage law, equations for the magnetic flux are established.

$$\begin{cases} R_{ai}\phi_{ai} + R_{si}\phi_i + R_{ai+1}\phi_{ai+1} + R_{ei}\phi_{ei} = \theta_i + \theta_{i+1} - \theta_{p,i} \\ R_{li}\phi_{li} + R_{ei}\phi_{ei} = \theta_i + \theta_{i+1} - \theta_{p,i} \end{cases} \quad (1)$$

Equation (1) is expressed in matrix and vector form.

$$\mathbf{A}\,\boldsymbol{\phi} = \mathbf{T}^{T}\boldsymbol{\theta} - \mathbf{T}_{e}{}^{T}\boldsymbol{\theta}_{p} \tag{2}$$

where the reluctance matrix $\mathbf{A} \in R^{12\times 12}$ and

$$\mathbf{A} = \begin{bmatrix} R_{a1}+R_{a2}+R_{s1}+R_{e1} & R_{e1} & R_{a2} & 0 & 0 & \cdots \\ R_{e1} & R_{l1}+R_{e1} & 0 & 0 & 0 & \cdots \\ R_{a2} & 0 & R_{a2}+R_{a3}+R_{s2}+R_{e2} & R_{e2} & R_{a3} & \cdots \\ 0 & 0 & R_{e2} & R_{l2}+R_{e2} & 0 & \cdots \\ \vdots & \vdots & \vdots & \vdots & \vdots & \ddots \end{bmatrix}$$

4.2. Reluctant Calculation

Based on the method in Refs. [22,23] and Figure 5, the reluctances in the EMC can be calculated.

1. The air gap reluctance can be calculated by the following formula.

$$\Lambda_{aj} = \frac{1}{R_{aj}} = \frac{1}{R_{a,mj}} + \frac{1}{R_{a,nj}} + \frac{1}{R_{a,Lj}} \tag{3}$$

where Λ_{aj} and R_{aj} are the magnetic permeance and reluctance of the air gap, respectively. To fit the magnetic flux fluctuation caused by the tooth-slot effect, first and second harmonics are selected and added to the magnetic permeance. Λ_{aj} and $R_{a,mj}$ are the reluctances corresponding to the main magnetic flux. $R_{a,nj}$ is the reluctance corresponding to the slot magnetic flux. $R_{a,Lj}$ is the reluctance corresponding to the LIG magnetic flux, and each type of reluctance can be calculated using the following formula.

$$R_{a,xj} = \frac{s_j + h_{xj}}{\mu_0 A_{a,xj}},\ x \in [m,n,L] \tag{4}$$

where s_j is the air gap between the magnet pole and the long stator tooth. μ_0 is the air permeability. $A_{a,xj}$ is the corresponding air gap area and h_{xj} is the additional air gap length.

2. Magnetic leakage reluctance between adjacent magnet poles can be calculated by the following formula.

$$R_{li} = \frac{h_{li}}{\mu_0 A_{li}} \tag{5}$$

where A_{li} is the equivalent air gap area and h_{li} is the equivalent air gap length between adjacent magnetic poles.

3. The reluctances of the stator core, pole core, and yoke can be calculated via segments, and the sectional area of each segment should be as similar as possible. The specific sections are shown in Figure 11, where the pole core and yoke are divided into five sections and the stator core is divided into three sections. The nonlinearity of magnetic materials is considered in the reluctance calculation.

   The reluctance of the pole core and yoke can be expressed as

$$R_{ei} = \sum_{k=1}^{5} \frac{l_{ei,k}}{\mu_0 \mu_r(\phi_{ei,k}) A_{ei,k}} \tag{6}$$

   The reluctance of the stator core can be expressed as

$$R_{si} = \sum_{k=6}^{8} \frac{l_{si,k}}{\mu_0 \mu_r(\phi_{si,k}) A_{si,k}} \tag{7}$$

where $l_{ei,k}$ and $l_{si,k}$ are the lengths of each segment of iron core at the side of the levitation magnet and the long stator, respectively. $A_{ei,k}$ and $A_{si,k}$ are the sectional areas of each segment of iron core at the side of the levitation magnet and the long stator. μ_r is the relative permeability of each segment of iron core. In order to introduce the nonlinear characteristics of magnetic materials into the EMC model, the relative permeability μ_r is no longer a constant value, which can be calculated according to [28].

$$\mu_r(\phi_{ei}, k) = \frac{1}{\mu_0(\alpha_1 + \alpha_2(\frac{\phi_{ei}}{A_{ei,k}})^{\alpha_3 - 1})} \tag{8}$$

Therefore, the reluctance matrix **A** related to the gap s_j and magnetic flux ϕ_i can be recorded as $\mathbf{A}(s,\phi)$.

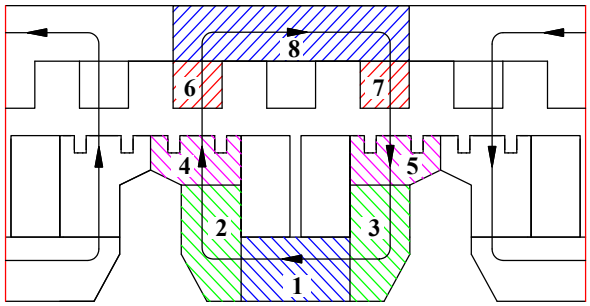

Figure 11. Magnetic material segments.

4.3. Magnetic Flux and Force

In the circuit of the damper coil, the relationship between the inductive current I_{pi} and magnetic flux ϕ_{ei} can be established.

$$I_{pi} = \frac{n_p}{R_{dp}}\dot{\phi}_{ei} \tag{9}$$

Equation (2) can be expressed as

$$\mathbf{A}(s,\phi)\boldsymbol{\phi} = nI\mathbf{T}^T\boldsymbol{N} - \frac{{n_p}^2}{R_{dp}}{\mathbf{T}_e}^T\dot{\boldsymbol{\phi}}_e \tag{10}$$

where the vector $\boldsymbol{N} = [1, 1, 1, 1, 1, 1, 1]^T$. According to the relationship of magnetic fluxes $\boldsymbol{\phi_e} = \mathbf{T_e}\boldsymbol{\phi}$, Equation (10) is derived as

$$\boldsymbol{\phi}_e = nI\mathbf{T}_e\mathbf{A}^{-1}(s,\phi)\mathbf{T}^T\boldsymbol{N} - \frac{{n_p}^2}{R_{dp}}\mathbf{T}_e\mathbf{A}^{-1}(s,\phi){\mathbf{T}_e}^T\dot{\boldsymbol{\phi}}_e \tag{11}$$

To simplify the expression, $\mathbf{T_e}\ \mathbf{A}^{-1}(s,\phi)\ {\mathbf{T_e}}^T$ is recorded as a matrix $\mathbf{M}^{-1}(s,\phi)$ and $\mathbf{T_e}\ \mathbf{A}^{-1}(s,\phi)\ \mathbf{T}^T\boldsymbol{N}$ is recorded as a matrix $\mathbf{P}(s,\phi)$. Then, the explicit differential equation on variable $\boldsymbol{\phi_e}$ can be expressed as

$$\dot{\boldsymbol{\phi}}_e = \frac{R_{dp}}{{n_p}^2}\mathbf{M}(s,\phi)(nI\mathbf{P}(s,\phi) - \boldsymbol{\phi}_e) \tag{12}$$

Combining Equations (9), (10), and (12), the magnetic fluxes $\boldsymbol{\phi}$ and $\boldsymbol{\phi_e}$ and inductive current I_{pi} can be solved, and then all the magnetic flux vectors can be obtained. Based on the virtual work principle, the magnetic force of each magnet pole can be calculated using the following formula.

$$F_{mag,j} = \frac{{\phi_{aj}}^2}{2\mu_0 A_{aj}} \tag{13}$$

Therefore, the magnetic force of half levitation magnet is calculated as

$$F_{mag} = \sum_{j=1}^{6} F_{mag,j} \tag{14}$$

5. Analysis and Validation

As depicted in Figure 12, a 2D FEM model of the magnet and long stator is established to verify the EMC model and ensure the accuracy of the analysis. For the magnet and long stator, the 2D FEM model can achieve reasonable accuracy due to the uniformity of their cross-section and improve the calculation efficiency. The magnetic flux fluctuations caused by the tooth-slot effect are considered in the EMC and FEM models. The main parameters utilized in both models are detailed in Table 1. For these simulations, the loop current is set to a nominal value of 25 A, with an operating speed of 600 km/h.

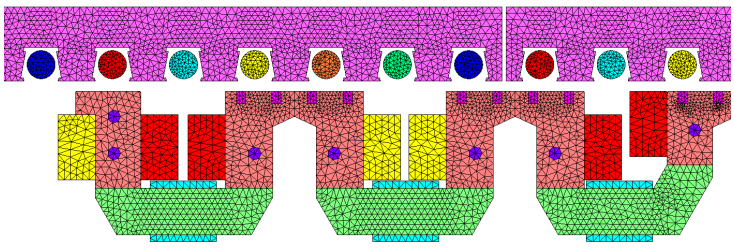

Figure 12. Two-dimensional partial finite element model.

Table 1. Parameters of the magnet and long stator.

Parameter	Value
Stator polar distance	258 mm
Magnet polar distance	266.5 mm
Width of stator tooth	43 mm
Width of stator slot	43 mm
Thickness of iron core	170 mm
Turns of coil, n	300
Turns of damping coil, n_p	30
Resistance, R_{dp}	1.5 Ω
Loop current, I	25 A
Operating speed	600 km/h
Mechanical gap	9 mm

5.1. Magnetic Flux and Inductive Current of Damping Coil

The calculation results of the magnetic flux ϕ_{p4} in the magnetic yoke between magnet poles no. 4 and no. 5 are illustrated in Figure 13. In Figure 13a, there is a large fluctuation range of 0.17~0.375 Wb for the magnetic flux ϕ_{p4} of the existing magnet without damping coils. The maximum peak-to-peak value is 0.205 Wb and the proportion of fluctuation is as high as 37.6%. In Figure 13b, the magnetic flux ϕ_{p4} of the novel magnet with damping coils calculated by both models has a high consistency and the maximum error is only about 2%. The magnetic flux fluctuation range is 0.255~0.31 Wb and the maximum peak-to-peak value is 0.055 Wb, which is far lower than the existing magnet. The proportion of fluctuation is notably reduced to 9.7%. This illustrates that the damping coils are beneficial for suppressing magnetic flux fluctuation. Consequently, it can be inferred that the inductive voltage will reduce simultaneously.

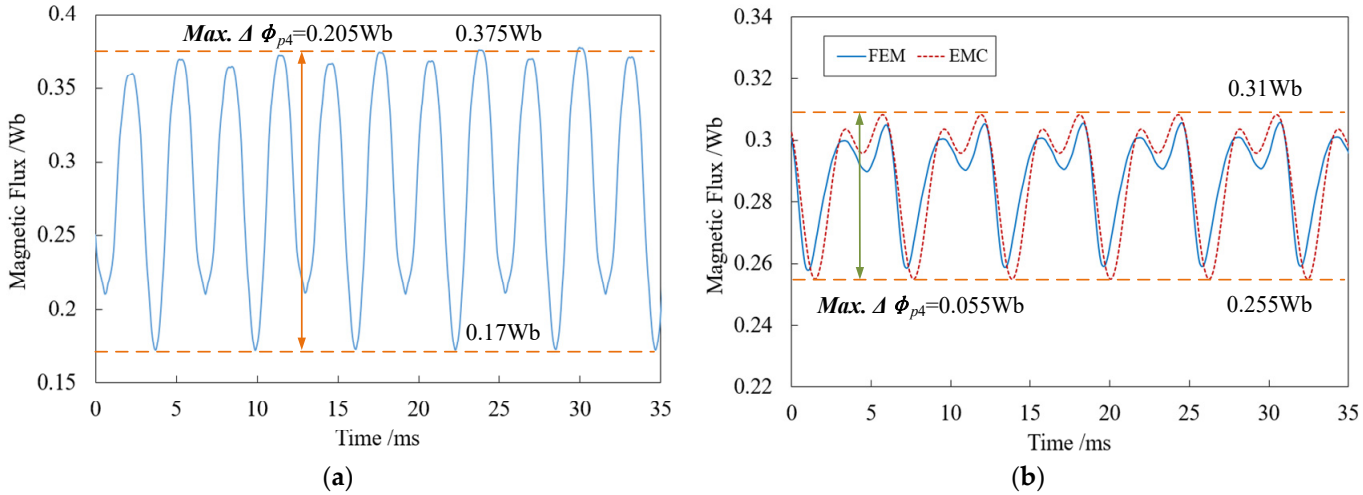

Figure 13. Magnetic flux ϕ_{p4} of magnetic yoke: (**a**) no damping coils; (**b**) with damping coils.

The inductive current of the damping coil corresponding to the magnetic flux ϕ_{p4} is also calculated by both models, as pictured in Figure 14. The EMC result is similar to that of the FEM, with only a slight phase deviation. The upper peak value is less than 40 A, while the lower peak value is about −20 A. The effective value is approximately 14.5 A. Considering the current-carrying capacity of copper, it is sufficient to design the cross-sectional area of copper-enameled wire applied for damping coils to be over 2 mm^2. As for the resistor connected in series with damping coil, they are installed on the surface of the box girder and dissipate heat through high-speed running winds. From the perspective of engineering applications, it is practical to apply the novel magnet with damping coils in a high-speed maglev train.

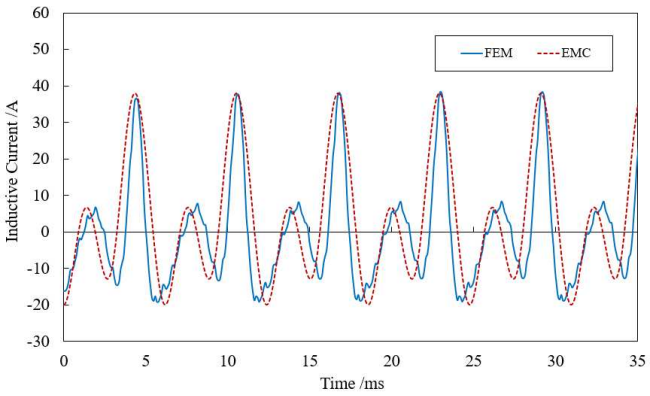

Figure 14. Inductive current of damping coil no. 4.

5.2. Magnetic Force of Magnet

To study the magnet characteristics, a magnet test platform, depicted in Figure 15, is constructed. The gap between the magnet and long stator is adjusted and maintained by the hydraulic system. The loop current ranges from 0 to 50 A, with increments of 5 A. The magnetic force is measured by the force sensor.

Figure 16 portrays the relationship between the static magnetic force and the loop current under different mechanical gaps. Throughout the entire current range, the static magnetic force results of EMC are closely aligned with those from the FEM and experimental tests when considering the nonlinearity of magnetic materials. With increasing currents, the static magnetic force exhibits a saturation phenomenon in the high current range. For the levitation magnet of the high-speed maglev train, the nominal mechanical gap is set

to 9 mm and the nominal loop current is 25 A. At this moment, the calculated and tested magnetic force is about 45 kN.

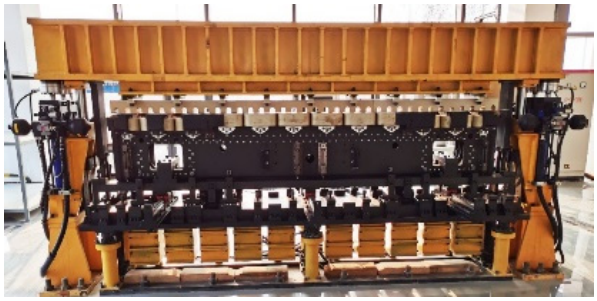

Figure 15. Magnet test platform.

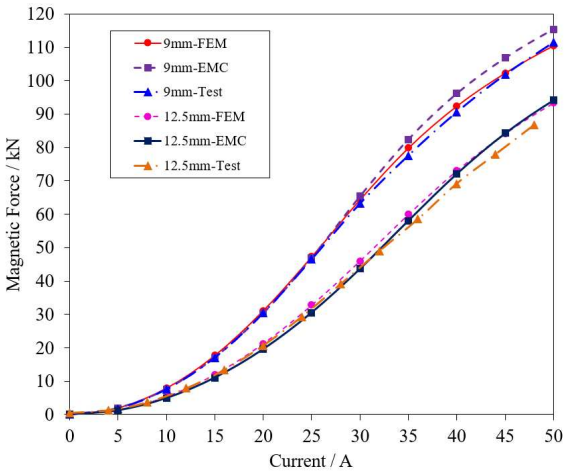

Figure 16. Static magnetic force characteristics.

Dynamic magnetic forces are analyzed by both of the models as well, as shown in Figure 17. The overall magnetic force trends of the both models are similar, with average hovering around 45 kN. However, there is a higher frequency fluctuation in the FEM results compared to the EMC results. This discrepancy arises from the fact that, as mentioned earlier, only first and second harmonics are selected and added to the magnetic permeance between the magnet pole and the long stator. In fact, the tooth-slot effect can generate multiple harmonics.

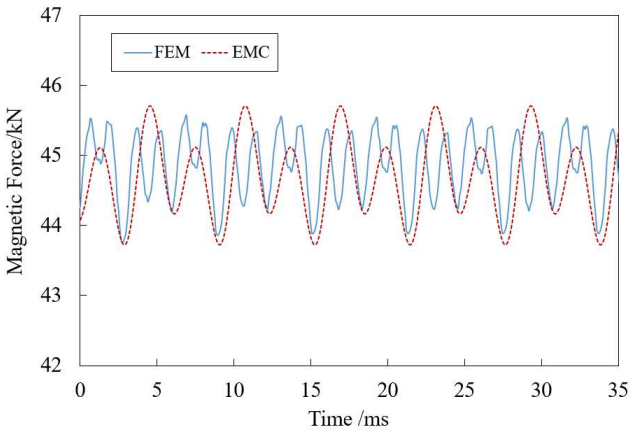

Figure 17. Dynamic magnetic force characteristics.

5.3. Inductive Voltage of Magnet Pole

To verify the inference that the damping coil can effectively suppress the inductive voltage of the magnet pole, the damping coils are incorporated in to the equivalent ground test equipment, as shown in Figure 18, and the inductive voltage of the magnet pole is retested under the same power supply conditions as before. The inductive voltage test result is shown in Figure 19, and comparisons between the existing magnet and the novel magnet are summarized in Table 2. The maximum upper and lower peaks are 0.5 kV and −0.6 kV, respectively, with a maximum peak-to-peak value of U_{pp} 1.1 kV, which has dramatically reduced compared to the existing magnet and been far below the voltage withstand test standard of 2.5 kV. As a consequence, the risk of magnet pole insulation failure is significantly reduced. From a practical perspective, damping coils can protect the insulation of the magnet pole from overvoltage by suppressing high-frequency magnetic flux fluctuation, thereby enhancing the service life of the levitation magnet.

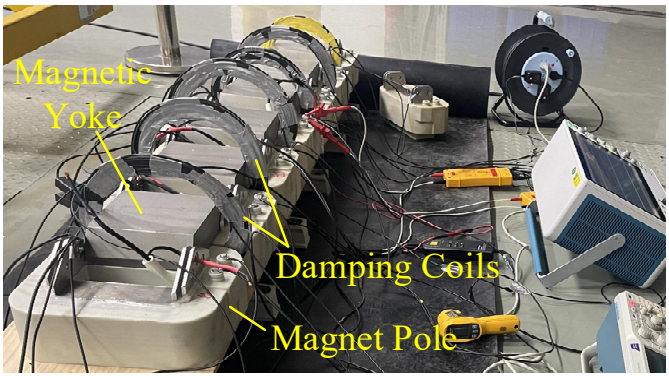

Figure 18. Equivalent ground test with damping coils.

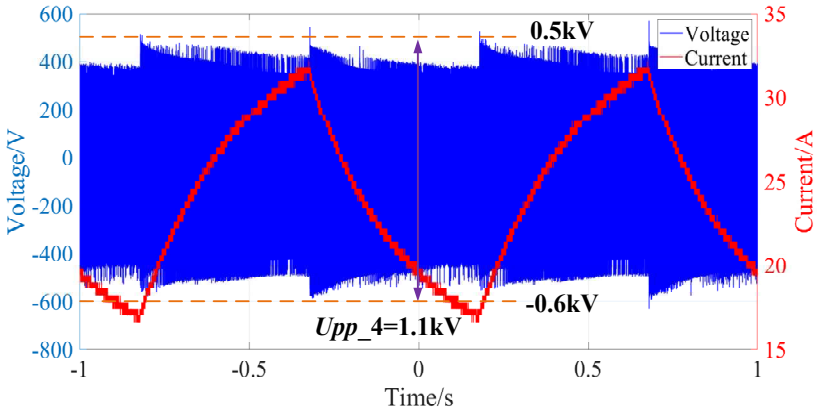

Figure 19. Inductive voltage with damping coils.

Table 2. Analysis comparisons of the existing and novel magnets.

Analysis Results	No Damping Coil	With Damping Coil
Upper peak of magnetic flux, ϕ_{p4}/Wb	0.375	0.31
Lower peak of magnetic flux, ϕ_{p4}/Wb	0.17	0.255
Maximum value of $\Delta\phi_{p4}$/Wb	0.205	0.055
Upper peak of inductive voltage/kV	2.6	0.5
Lower peak of inductive voltage/kV	−2.9	−0.6
Maximum value of U_{pp}/kV	5.5	1.1

6. Conclusions

In this paper, a novel levitation magnet with damping coil used for high-speed maglev train is designed, with accurately established EMC and FEM models. To validate the results, numerous experiments are performed. Based on the analysis of the magnetic flux, inductive current, magnetic force, and inductive voltage, the following conclusions are drawn.

(1) The nonlinearity of magnetic materials and magnetic flux fluctuation caused by the tooth-slot effect is taken into consideration in the EMC model. This enables the efficient and accurate analysis of magnetic characteristics. Therefore, it offers greater convenience for subsequent optimization design and joint simulation with control models, facilitating the analysis of dynamic levitation performance. (2) The magnetic flux fluctuation of the novel magnet with damping coils is significantly reduced, only about 26.8% of the existing magnet. It indicates that the damping coils can effectively suppress the magnetic flux fluctuation resulting from the tooth-slot effect. The effective value of the inductive current is about 20 A, which is reasonable for the current-carrying capacity of the damping coil. (3) Under the influence of magnetic flux fluctuation suppression, the inductive voltage of the novel magnet with damping coils is considerably lowered, with a peak-to-peak voltage value of only about 1.1 kV. This value is far below the withstand voltage test standard of the insulation layer on the surface of the iron core. It is extremely beneficial for improving the operational safety and service life of the levitation magnet.

Author Contributions: Conceptualization, Z.D.; Methodology, W.H.; Validation, X.G.; Formal analysis, S.F.; Writing—review & editing, Y.Z. All authors have read and agreed to the published version of the manuscript.

Funding: This work was co-supported by the National Key R&D Program of China under grant number 2023YFB4302500, the Sichuan Science and Technology Program (2023ZYD0021 and 2022JDTD0011), the Fundamental Research Funds for the Central Universities of China (2682023CG010), and the State Key Laboratory of High-Speed Maglev Transportation Technology (SKLM-SFCF-2023-008).

Institutional Review Board Statement: Not applicable.

Informed Consent Statement: Not applicable.

Data Availability Statement: The data presented in this study are available on request from the corresponding author.

Conflicts of Interest: Authors Shanqiang Fu, Weitao Han, Xinmai Gao and Ying Zhou were employed by the company CRRC Qingdao Sifang Company Ltd. The remaining authors declare that the research was conducted in the absence of any commercial or financial relationships that could be construed as a potential conflict of interest.

References

1. Han, B.C.; He, Z.; Wen, T.; Zheng, S.Q. Design, optimization and test of RHMB considering dynamic characteristics. *Int. J. Mech. Sci.* **2023**, *238*, 107847. [CrossRef]
2. Tang, J.; Zhang, M.; Cui, X.; Sun, J.; Zhou, X. Neural Network Sliding Model Control of Radial Translation for Magnetically Suspended Rotor (MSR) in Control Moment Gyro. *Actuators* **2023**, *12*, 217. [CrossRef]
3. Xu, S.; Li, J.; Wang, Z.; Sun, J.; Ren, H. Integrated Radial-axial Magnetic Bearing with Variable Permanent-Magnet Bias Flux In Situ. *J. Electr. Eng. Technol.* **2024**, *19*, 2447–2455. [CrossRef]
4. Dai, M.; Zhang, Z.-W.; Dorjoy, M.M.H.; Zeng, L. Analysis and optimization of vibration and noise of high-speed magnetic suspension motor. *J. Low Freq. Noise Vib. Act. Control* **2022**, *41*, 625–636. [CrossRef]
5. Liang, J.Y. Development status and future prospects of the high-speed maglev transportation system in China. *Science* **2022**, *74*, 31–36+2+69.
6. Lee, H.-W.; Kim, K.-C.; Lee, J. Review of maglev train technologies. *IEEE Trans. Magn.* **2006**, *42*, 1917–1925.
7. Lin, G.B.; Liu, W.M.; Li, H.T.; Xu, J.Q.; Sun, Y.G. Opportunities and Challenges for the Development of High-speed Maglev Transportation in China. *Sci. Technol. Foresight* **2023**, *2*, 7–18.
8. Yan, L.G. Development and application of the Maglev transportation system. *IEEE Trans. Appl. Supercond* **2008**, *18*, 92–99.
9. Liang, X.; Jiang, T.Y.; Hong, Y.; Zhang, J.B.; Jiang, M.; Wang, Z.Y. Vibration Response Analysis of Simply Supported Box Girder Bridge-Maglev Train in Accelerated Test of Changsha Maglev Express. *Adv. Mater. Sci. Eng.* **2020**, *2020*, 9563747. [CrossRef]

10. Xu, J.Q.; Chen, C.; Sun, Y.G.; Rong, L.J.; Lin, G.B. Nonlinear Dynamic Characteristic Modeling and Adaptive Control of Low Speed Maglev Train. *Int. J. Appl. Electromagn. Mech.* **2019**, *62*, 73–92. [CrossRef]
11. Ding, J.; Yang, X.; Long, Z. Structure and control design of levitation electromagnet for electromagnetic suspension medium-speed maglev train. *J. Vib. Control* **2019**, *25*, 1179–1193. [CrossRef]
12. Chaban, A.; Lukasik, Z.; Lis, M.; Szafraniec, A. Mathematical Modeling of Transient Processes in Magnetic Suspension of Maglev Trains. *Energies* **2020**, *13*, 6642. [CrossRef]
13. Cui, L.B.; Ma, G.T.; Su, Z.H.; Li, J.; Feng, P.; Guo, M.; Zhao, J.; Luo, J. Partial Force Calculation and Structural Strength Analysis of Null-Flux Coil for Superconducting Electrodynamic Suspension Train. *IEEE Trans. Appl. Supercond.* **2024**, *34*, 1–10. [CrossRef]
14. Luo, J.; Cui, L.B.; Su, Z.H.; Li, Y.X.; Li, J.; Zhu, Z.X.; Ma, G.T. Design Optimization of Null-Flux Superconducting Electrodynamic Suspension for Cost-Saving and Performance Improvement. *IEEE/ASME Trans. Mechatronics* **2023**, *28*, 3502–3512. [CrossRef]
15. Sun, Y.; Qiang, H.; Wang, L.; Ji, W.; Mardani, A. A Fuzzy-Logic-System-Based Cooperative Control for the Multielectromagnets Suspension System of Maglev Trains With Experimental Verification. *IEEE Trans. Fuzzy Syst.* **2023**, *31*, 3411–3422. [CrossRef]
16. Xu, Y.L.; Wang, Z.L.; Li, G.Q.; Chen, S.W.; Yang, Y.B. High-speed running maglev trains interacting with elastic transitional viaducts. *Eng. Struct.* **2019**, *183*, 562–578. [CrossRef]
17. He, Y.; Wu, J.; Xie, G.; Hong, X.; Zhang, Y. Data-driven relative position detection technology for high-speed maglev train. *Measurement* **2021**, *180*, 109468. [CrossRef]
18. Sun, Y.; He, Z.; Xu, J.; Li, F.; Zhang, D. Cooperative Model Predictive Levitation Control for Two-Points Electromagnetic Levitation System of High-Speed Maglev Vehicle. *IEEE Trans. Intell. Veh.* **2023**, *1*, 1–12. [CrossRef]
19. Zhang, T.; Shen, D.; Jiang, S.; Xu, H. Adaptive Fixed-Time Antilock Control of Levitation System of High-Speed Maglev Train. *IEEE Trans. Intell. Veh.* **2023**, *8*, 3394–3404. [CrossRef]
20. Li, Q.; Hu, Y.; Wu, H. Structure Design and Optimization of the Radial Magnetic Bearing. *Actuators* **2023**, *12*, 27. [CrossRef]
21. Sun, J.J.; Ju, Z.Y.; Peng, C.; Le, Y.; Ren, H.L. A Novel 4-DOF Hybrid Magnetic Bearing for DGMSCMG. IEEE Trans. *Ind. Electron.* **2017**, *64*, 2196–2204. [CrossRef]
22. Schmid, P.; Schneider, G.; Dignath, F.; Liang, X.; Eberhard, P. Static and Dynamic Modeling of the Electromagnets of the Maglev Vehicle Transrapid. *IEEE Trans. Magn.* **2021**, *57*, 1–15. [CrossRef]
23. Fu, S.Q.; Wu, D.H.; Han, W.T.; Zhou, Y. Modeling and Analysis of Magnet for Maglev Train Based on Nonlinear Material. *J. Southwest Jiaotong Univ.* **2023**, *58*, 779–885.
24. Zaccardo, V.M.; Buckner, G.D. Active magnetic dampers for controlling lateral rotor vibration in high-speed rotating shafts. *Mech. Syst. Signal Process.* **2021**, *152*, 107445. [CrossRef]
25. Fang, J.; Le, Y.; Sun, J.; Wang, K. Analysis and Design of Passive Magnetic Bearing and Damping System for High-Speed Compressor. *IEEE Trans. Magn.* **2012**, *48*, 2528–2537. [CrossRef]
26. Zhang, P.; Zhao, J.; Li, H.; Ren, T.; Ke, Z.; Deng, Z. Vibration Reduction Using Eddy Current Damper in High-Temperature Superconducting Maglev System. *J. Supercond Nov. Magn.* **2022**, *35*, 87–94. [CrossRef]
27. Zhang, P.; Deng, Z.; Liang, L.; Wang, L.; Ke, Z.; Lv, C.; Li, Z.; Wu, X. Vibration Suppression of HTS Maglev System Based on Negative Resistance Electromagnetic Shunt Damper. *IEEE Trans. Appl. Supercond.* **2022**, *32*, 1–5. [CrossRef]
28. Polinder, H.; Slootweg, J.G.; Hoeijmakers, M.J.; Compter, J.C. Modelling of a linear PM machine including magnetic saturation and end effects: Maximum force to current ratio. *IEEE Trans. Ind. Appl.* **2003**, *39*, 1681–1688. [CrossRef]